Opto-Electronic Technology

CN 51-1811/O4 ISSN (Print) 2097-6003 ISSN (Online) 2097-8006

Dual quasi-BIC resonances synergized laser cooling in halide perovskite metasurface

Ying Che, Peng Lu, Yang Li, Junhao Zeng, Mengxia Hu, Fei Qin*, Tianyue Zhang* and Xiangping Li*

Citation: Che Y, Lu P, Li Y, Zeng JH, Hu MX, Qin F, Zhang TY, Li XP. Dual quasi-BIC resonances synergized laser cooling in halide perovskite metasurface. *Opto-Electron Technol* **2**, 250013 (2026).

https://doi.org/10.29026/oet.2026.250013

Received: 14 December 2025; Accepted: 23 January 2026; Published online: 12 February 2026

OET | Opto-Electronic Technology

Article

March 2026, Vol. 2, No. 1

Open Access

Dual quasi-BIC resonances synergized laser cooling in halide perovskite metasurface

Ying Che[1,2], Peng Lu[3], Yang Li[1,2], Junhao Zeng[1,2], Mengxia Hu[1,2], Fei Qin[1,2]*, Tianyue Zhang[3,4]* and Xiangping Li[1,2]*

Abstract: Halide perovskites, recognized for efficient upconversion photoluminescence and high quantum yields, present a promising platform for laser refrigeration. Their high refractive index further enables the design of nanostructures that support strong Mie-type resonances, leading to subwavelength light confinement and enhanced laser cooling performance. In this work, we theoretically propose and numerically demonstrate a metasurface composed of nanostructured halide perovskite with tailored asymmetry, supporting dual-band quasi-bound states in the continuum (q-BICs) that simultaneously enhance optical excitation and upconversion photoluminescence. The perovskite metasurface exhibits a significant enhancement in optical absorption compared with the unpatterned perovskite film, along with a pronounced Purcell effect at the emission wavelength. Thermodynamic modelling further indicates net cooling down to –201 °C from room temperature under continuous laser illumination, exceeding the liquid-nitrogen cooling threshold. These findings establish design principles for mechanically refrigerant-free thermal management and open a pathway toward integrated cryogenic photonic platforms.

Keywords: laser cooling; bound states in the continuum; perovskite metasurfaces

DOI: 10.29026/oet.2026.250013 | CSTR: 32419.14.oet.2026.250013

Citation: Che Y, Lu P, Li Y et al. Dual quasi-BIC resonances synergized laser cooling in halide perovskite metasurface. *Opto-Electron Technol* **2**, 250013 (2026).

1 Introduction

The miniaturization of micro- and nano-optoelectronic devices has led to exponential growth in power and thermal flux densities, exceeding the limits of conventional thermal management. Bulk material constraints and vibration sensitivity further undermine precision thermal control in submicron architectures. Anti-Stokes fluorescence cooling has emerged as a transformative solid-state refrigeration technology. It operates entirely optically, is vibration-free, produces no electromagnetic interference, and offers high reliability, making it a promising solution for nanoscale thermal management[1–3]. This cooling mechanism relies on anti-Stokes photoluminescence, where pump photons with energy slightly below the mean fluorescence energy are absorbed together with lattice phonons, the subsequent emission of higher-energy photons converts thermal energy stored in phonons into radiation and transfers entropy from the lattice to the optical field[4]. The concept was first proposed by Pringsheim P in 1929[5] and later formalized by Landau. In 1995, Epstein RI et al. demonstrated a 0.3 K temperature drop in Yb^{3+}-doped ZBLANP glass, proving the feasibility of solid-state refrigeration[6]. Subsequent improvements through fiber geometry optimization and phonon-assisted transitions were demonstrated to enhance the cooling efficiency[7–11]. However, the phonon-assisted upconversion efficiency in rare-earth systems suffers a drastic reduction below 90 K[12,13], where the greatly reduced phonon population and increasingly stringent requirements on external quantum efficiency make further cooling highly inefficient.

Semiconductors offer a prospective platform that

Received: 14 December 2025

Accepted: 23 January 2026

Published online: 12 February 2026

[1]Guangdong Provincial Key Laboratory of Optical Fiber Sensing and Communications, Institute of Photonics Technology, College of Physics & Optoelectronic Engineering, Jinan University, Guangzhou 510632, China; [2]International Cooperation Joint Laboratory for Optoelectronic Hybrid Integrated Circuits, Jinan University, Guangzhou 510632, China; [3]School of Integrated Circuits, Beijing University of Posts and Telecommunications, Beijing 100876, China; [4]State Key Laboratory of Information Photonics and Optical Communications, Beijing 100876, China.

*Correspondence: F Qin, qinfei@jnu.edu.cn; TY Zhang, tianyue_zhang@bupt.edu.cn; XP Li, xiangpingli@jnu.edu.cn

overcomes this thermal constraint. Their superior photon harvesting properties and capability for cryogenic operation extend the achievable cooling range deep into the cryogenic regime. This potential was realized with CdS nanobelts that achieved 40 K of net cooling via Fröhlich phonon coupling in 2013[14]. Later, core-shell quantum dots (e.g., CdSe/ZnS) reached near-unity quantum efficiency by suppressing photon reabsorption through interfacial engineering[15,16], making them promising candidates for nanoscale optical cooling. Nevertheless, nonradiative recombination induced by surface defects remains a major obstacle, often necessitating complex passivation strategies.

Lead halide perovskites have recently attracted significant attention in optical refrigeration[17,18]. Their strong electron-phonon coupling supports multiphonon annihilation, a quantum mechanical prerequisite for local entropy reduction. Crucially, perovskites exhibit innate structural defect tolerance, which effectively mitigates nonradiative losses that historically limited cooling performance. These properties offer new pathways to address photon entropy compensation challenges in anti-Stokes refrigeration systems. In 2016, Ha ST et al. demonstrated phonon-assisted upconverted emission in perovskites[19], achieving net cooling of 23 K in bulk $MAPbI_3$ crystals and 58 K in 2D $PhEPbI_4$ nanoplatelets. Such advances propel perovskite-based refrigeration as a competitive technology for cryogenic applications previously dominated by rare-earth materials. Additionally, the high refractive indices of perovskites (n~2.0–2.5) enable strong Mie resonances, revolutionizing the design in perovskite photonic devices[20–24]. These resonances facilitate sub-100-nm light confinement through multipolar scattering and bandgap tuning in photonic crystals. Integrating Mie-type metamaterials with halide perovskites has demonstrated exceptional performance enhancements in photodetectors[25,26], photovoltaics[27,28], and nanolasers[22,29–31]. This nanoscale synergy reveals that nanophotonic engineering could fully unlock the potential of perovskites for optical refrigeration, particularly through resonant entropy control.

Photonic bound states in the continuum (BICs)[32–39] offer a powerful mechanism for enhancing optical refrigeration. The BICs suppress radiative leakage and support extremely high quality (high-Q) resonances[40–42], thereby strengthening photon-exciton-phonon interactions essential for efficient cooling. Building on this concept, in this work, we theoretically demonstrate a resonance engineering strategy based on $MAPbBr_3$ ($CH_3NH_3PbBr_3$) perovskite metasurfaces that synergistically enhances both optical absorption and emission. By incorporating dual quasi-BIC resonances to match the excitation and emission wavelength bands, the metasurfaces achieve an exceptionally large photon absorption cross-section (4.3×10^{-14} m^2 at 625 nm) together with a Purcell factor as high as 8.2 at emission wavelength of 540 nm via localized density-of-states engineering. These synergistic effects deliver an external quantum efficiency (EQE) of 98.8% under an illumination intensity of 1.5×10^5 W/cm^2. Concurrently, anti-Stokes-mediated thermal suppression yields laser cooling down to −201 °C (72 K), surpassing the boiling point (77 K) of liquid nitrogen, and establishing a new paradigm for solid-state optothermal refrigeration. The proposed framework offers a viable pathway toward room-temperature nanoscale refrigeration, providing a fundamentally new strategy for thermal management in integrated optoelectronics systems.

2 Results and discussions

Figure 1 illustrates the working principle of the dual-band q-BIC perovskite metasurface for enhanced laser refrigeration. Laser refrigeration relies on three coupled processes as shown in Fig. 1(a): (I) absorption of low-energy pump photons, slightly below the emission energy, determined by the spectral overlap with material's absorption bands; (II) phonon-assisted energy upconversion, in which lattice phonons provide the energy difference between the absorbed pump photon and the emitted photon, governed by the material's band structure and phonon density of states; and (III) radiative emission of higher-energy photons, whose quantum yield depends on radiative recombination efficiency and defect-mediated nonradiative losses[3,43–45]. While process (II) is intrinsically determined by material properties, processes (I) and (III) can be precisely engineered by the photonic architectures through bandgap-tailored nanostructuring, allowing systematic optimization of absorption cross-sections and emission linewidths. Figure 1(b) shows the steady-state spectral characteristics of the organic-inorganic hybrid perovskite $MAPbBr_3$ ($CH_3NH_3PbBr_3$) film. Both the absorption spectrum (red curve) and photoluminescence spectrum (green curve) display characteristic band-edge transitions spanning 540–640 nm. The blue-shaded area indicates the theoretically predicted optical refrigeration window, derived from fundamental energy balance analysis accounting for Stokes shift constraints and intrinsic phonon scattering losses.

Figure 1(c) sketches the proposed perovskite metasurface composed of a hexagonal array of $MAPbBr_3$ perovskite nanodisks (green) on a glass substrate (gray) and encapsulated with a SiO_2-PDMS hybrid aerogel (refractive index 1.2) for environmental protection. A co-diagonal lateral displacement of the central disk within each unit cell, parameterized by ΔL (here defined such that $\Delta x = \Delta y = \Delta L = 70$ nm in Fig. 1(c)), introduces engineered in-plane symmetry breaking, converting ideal BICs (e.g., non-radiative dark modes) into leaky quasi-BICs (q-BICs) that sustain high Q-factors and intensified light-matter interactions. The metasurface is excited by an x-polarized incident light, and is designed to integrate two distinct q-BIC resonance channels: a long-wavelength mode (λ_1 = 625 nm) spectrally aligned with the absorption edge for optimized pump photon capturing, and a short-wavelength mode (λ_2 = 540 nm) matched to the

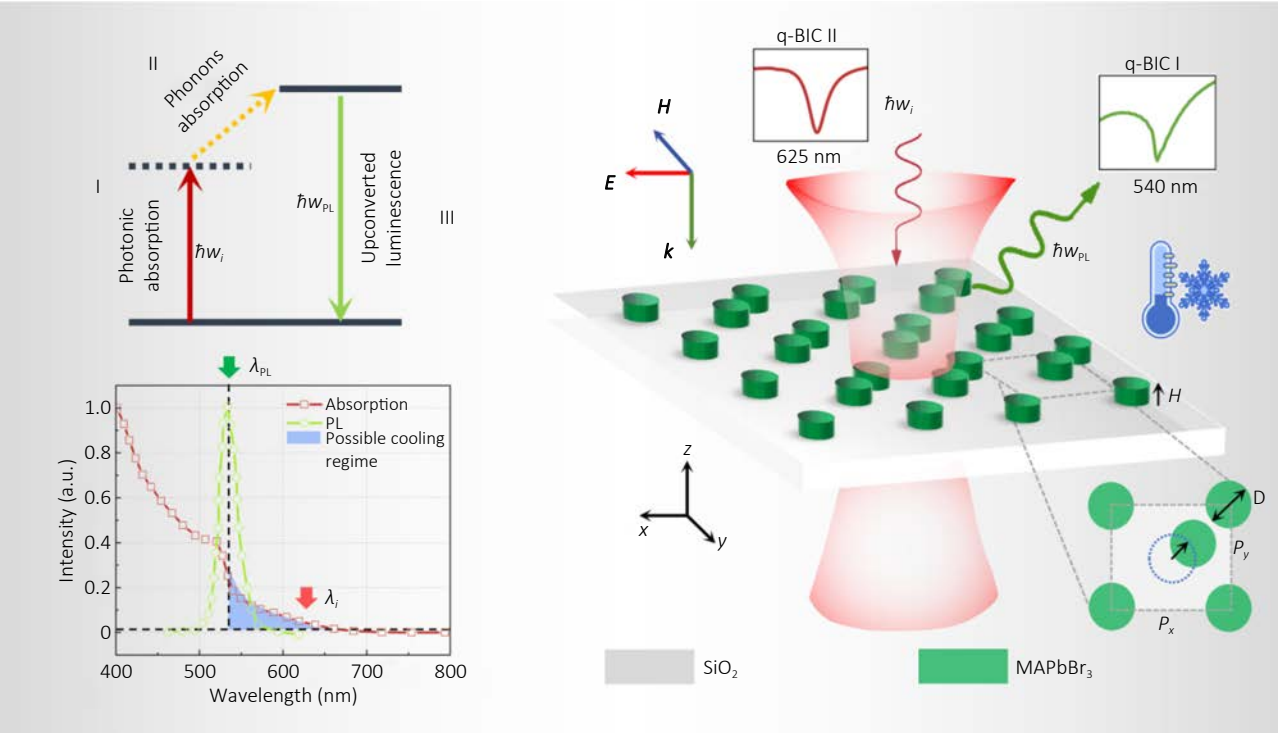

Fig. 1 | Dual-band q-BIC perovskite metasurface for laser refrigeration. (a) Energy diagram illustrating pump photon absorption ($\hbar w_i$), phonon-assisted energy uptake, and anti-Stokes emission ($\hbar w_{PL}$). (b) Absorption (red) and PL (green) spectra of $MAPbBr_3$ film with the shaded cooling window (540–640 nm). (c) Metasurface composed of hexagonal $MAPbBr_3$ nanodisks (radius = 85 nm, height = 200 nm) on glass and encapsulated with SiO_2-PDMS aerogel, arranged with lattice periods P_x = 420 nm and P_y = 375 nm, where a lateral offset $\Delta x = \Delta y = \Delta L$ =70 nm of the central disk breaks in-plane symmetry and produces two q-BIC resonances at λ_1 = 625 nm (pump absorption) and λ_2 = 540 nm (PL enhancement). The excitation light is linearly polarized along *x*-direction.

photoluminescence peak to boost radiative flux. Such coordinated resonance engineering mediates fluorescence cooling via phonon-bridged upconversion pathways, establishing a light-matter synergy that generates quantifiable surface temperature reduction under optical pumping.

The visible-range refractive indices of $MAPbBr_3$ perovskite (n~2.0–2.5), combined with its broadband absorption, establish a versatile photonic design paradigm for multi-wavelength resonant meta-devices. The wavelength-dependent optical constants $n(\lambda)$ and $k(\lambda)$ used in our simulations are shown in Section *4.6 Material parameters*. Through directional displacement engineering (Fig. 2(a–b)), wavelength-selective q-BIC excitation is achieved via independent position perturbations along the x and y directions: y-axis displacement (Δy) of the central perovskite disk in the metasurface unit induces a targeted optical resonance at the emission wavelength, while x-axis displacement (Δx) activates a distinct q-BIC mode precisely tuned to the excitation wavelength. Here, we use normally incident x-polarized excitation, which provides the strongest coupling, the response under y polarization is much weaker. Parametric scans in Fig. 2(c) confirm that coordinated diagonal displacements can concurrently activate dual-wavelength q-BIC resonances. Finite-difference time-domain (FDTD) simulations of electric field distributions (Fig. 2(d)) further reveal how orthogonal perturbations (Δy, Δx) and their combination reshape the electromagnetic profiles of the two q-BICs. For the unidirectional displacement with Δy = 70 nm and Δx = 70 nm, the 540 nm and 625 nm channels are excited separately with characteristic near-field symmetries, whereas for the diagonal case $\Delta x = \Delta y = \Delta L$ = 70 nm， the two channels coexist and partially hybridize, as indicated by the mixed edge- and center-localized hotspots. The theoretical quality factor (Q-factor) evolution of these dual-BIC modes, as a function of displacement values, is quantitatively summarized in Fig. 2(e). As shown in Fig. 2(e), the Q-factors of q-BIC-I and q-BIC-II decrease rapidly with increasing ΔL, reflecting the transition from symmetry-protected BICs to more strongly radiative leaky modes. Importantly, the choice of ΔL is not determined by maximizing Q alone, but by balancing mode excitability and resonance enhancement. Based on this trade-off, we use ΔL = 70 nm as a practical operating point for the subsequent analyses. The multipolar decomposition in Fig. 2(f) further confirm that both resonances originate from the interference between electric dipole, toroidal dipole, and quadrupole moments, in agreement with the near-field patterns in Fig. 2(d).

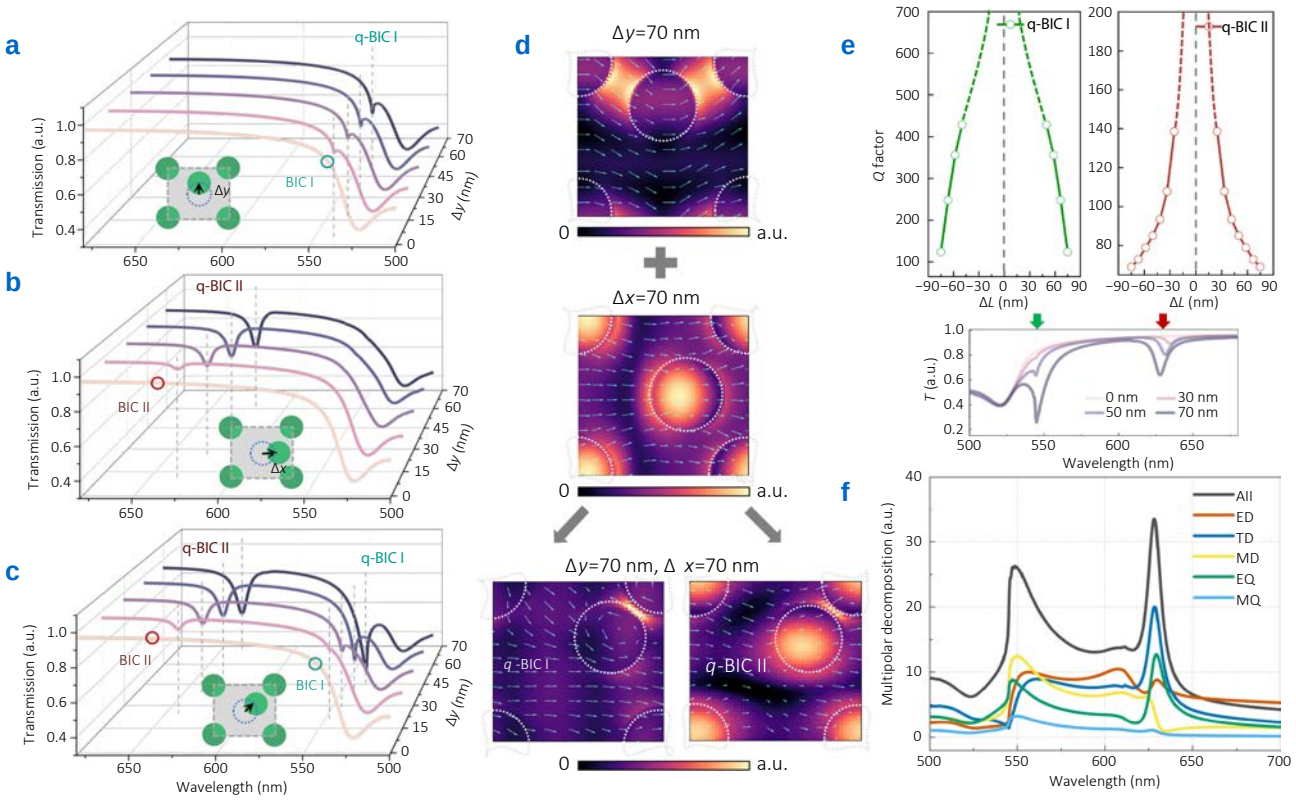

Fig. 2 | Dual-wavelength q-BIC formation in perovskite metasurfaces. (a–b) Transmission spectra showing q-BIC resonances near 540 nm and 625 nm, induced by central-disk displacements along the *y*-axis (Δ*y*) and *x*-axis (Δ*x*), respectively. (c) Calculated transmission spectra as a function of diagonal displacement Δ*L*, confirming the emergence of two separate q-BIC modes at 540 nm (q-BIC-I) and 625 nm (q-BIC-II). (d) Normalized near-field intensity distributions $|E|^2$ in the *x*-*y* plane through the disk center for three representative structures: Δ*y* = 70 nm, Δ*x* = 0 (top); Δ*x* = 70 nm, Δ*y* = 0 (middle) and Δ*x* = Δ*y* = Δ*L* =70 nm (bottom). The distinct spatial symmetries illustrate how the two q-BIC channels originate from orthogonal perturbations and hybridize when both are present. White arrows denote the in-plane electric-field vectors. (e) Simulated quality factors of q-BIC-I and q-BIC-II as functions of Δ*L*, with the inset showing representative transmission spectra. (f) Multipolar decomposition of perovskite metasurfaces in Cartesian coordinates.

The systematic investigation of the correlations among optical field characteristics, carrier dynamics, and cooling efficiency is shown in Fig. 3, which elucidates a pathway for optimizing the metasurface-based laser refrigeration system. The detailed calculation process is provided in the Methods section. The long-wavelength BIC resonance (mode q-BIC-II)can be steadily strengthened with increasing Δ*L* from 0 to 70 nm along the both orthogonal direction, leading to enhanced absorption cross-section around 625 nm (Fig. 3(a)). Meanwhile, the short-wavelength mode localization (mode q-BIC-I) will be intensified simultaneously that boosts the Purcell factor near 540 nm (Fig.3(b)). The synergistic dual-resonance coupling establishes an optimized energy conversion framework that critically enhances phonon-mediated upconversion efficiency.

To convert photonic field enhancement into functional cooling, the net cooling efficiency quantified as $\eta_C = \eta_{rad} \times (\lambda_i/\lambda_{PL}) - 1$, must be positive (i.e., net cooling $\eta_C > 0$). Equivalently, the system must satisfy the anti-Stokes criterion, requiring the external quantum efficiency (EQE) defined as $EQE = \eta_{rad} = R_{rad}^{eff}/(R_{rad}^{eff} + R_{nonrad})$ (where R_{rad}^{eff} and R_{nonrad} denote the radiative recombination rate and the non-radiative recombination rate, respectively), to exceed the threshold λ_{PL}/λ_i. This underlying mechanism involves spectral upconversion of absorbed low-energy photons (wavelength λ_i) to high-energy radiative states (λ_{PL}) via phonon-assisted processes, whereby the net photon energy gain counteracts lattice thermalization. Within this framework, excitation wavelength scanning in Fig. 3(c) maps the wavelength-dependent EQE threshold. For excitation at $\lambda_i = 625$ nm and emission at $\lambda_{PL} = 540$ nm, the threshold EQE is determined to be 86.4%, as indicated by the black arrow shown in Fig 3(c).

To achieve net cooling under operational conditions while satisfying the critical EQE threshold, we systematically investigated the competitive interplay among excitation power, carrier concentration, and EQE in the optimized structure with fixed Δ*L* of 70 nm. The carrier density at each excitation level was obtained by solving the steady-state rate equation using the calculated photogeneration rate and the recombination coefficients (the details is expressed as Eq. (4) in Methods section). As shown in the inset of

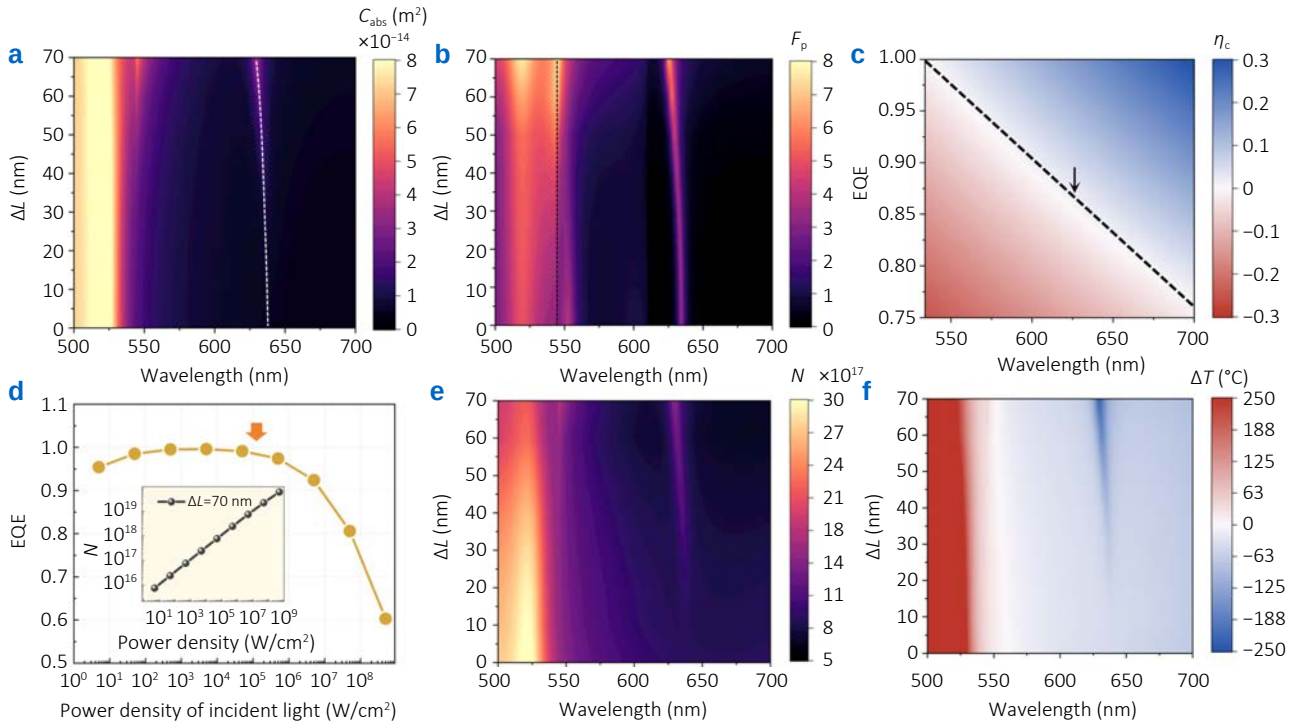

Fig. 3 | (a) Absorption cross-section (C_{abs}) as a function of wavelength and layer displacement Δ*L*. (b) Purcell factor (F_P) spectra versus wavelength and Δ*L*. (c) Cooling efficiency map showing the EQE threshold for net cooling. (d) EQE as a function of excitation power density, with inset showing the corresponding carrier concentration (*N*). (e) Carrier density distribution versus wavelength and Δ*L*. (f) Calculated steady-state temperature variation (Δ*T*) under different excitation wavelengths and Δ*L*.

Fig. 3(d), the carrier concentration increases monotonically from 7.61×10^{15} cm^{-3} to 6.04×10^{19} cm^{-3} as the excitation power rises from 5×10 W/cm² to 5×10^{8} W/cm². In contrast, the EQE exhibits a pronounced non-monotonic trend due to dynamic competition among recombination pathways. At low excitation powers (5×10 W/cm² ~ 5×10^{3} W/cm²), EQE increases from 95% to 98% as defect-state filling reduces the available non-radiative recombination channels. Within the intermediate power range (5×10^{4} W/cm² ~ 5×10^{6} W/cm²), EQE stabilizes near 99% as radiative recombination becomes dominant. However, under high-power excitation (>5×10^{6} W/cm²), the EQE declines to 60%, primarily due to Auger recombination and exacerbated thermalization losses. In this regime, the elevated carrier density promotes a three-body scattering process, where the energy released from electron-hole recombination is transferred to a third carrier rather than emitted as a photon. This non-radiative Auger mechanism dominates over radiative pathways, leading to significant efficiency degradation.

The operating point was strategically optimized at an excitation power density of 1.5×10^{5} W/cm² (corresponding to *EQE*= 98.8% and carrier concentration $N=1.3\times10^{18}$ cm^{-3}) to achieve an optimal trade-off between photonic cooling efficiency and thermal dissipation. At this operating condition, the dual-band q-BIC resonance coupling mechanism ensures a high EQE, which not only exceeds the anti-Stokes fluorescence threshold (86.4%) but also fulfills the critical criterion for net optical cooling. Excitation-wavelength-dependent temperature mapping (Fig. 3(f)) reveals localized deep-blue cooling zones with substantial temperature reduction exclusively under the theoretically optimized excitation wavelength (λ_i=625 nm). In contrast, non-resonant wavelengths exhibit weak thermal modulation (light-blue regions), confirming through simulation that the dual q-BIC resonances enable wavelength-selective energy extraction and suppression of thermal dissipation pathways within the designed framework.

Building on the wavelength-selective cooling mechanism established above, we further investigate the structural dependence of optothermal performance by systematically comparing three configurations (Fig. 4): (i) an unstructured perovskite film (thickness-matched to the metasurface), (ii) a symmetric metasurface (ΔL = 0), and (iii) an optimized dual-band q-BIC structure (ΔL = 70 nm). The symmetric metasurface (ΔL = 0 nm) supports a symmetry-protected BIC at normal incidence, so the far-field coupling to the radiative continuum is strongly suppressed by symmetry. Consequently, this configuration does not exhibit pronounced resonance-enhanced absorption under plane-wave excitation, and the Purcell-factor enhancement is much weaker than that in the symmetry-broken case over the 500–700 nm spectral window (Fig. 4(c)). Under intense

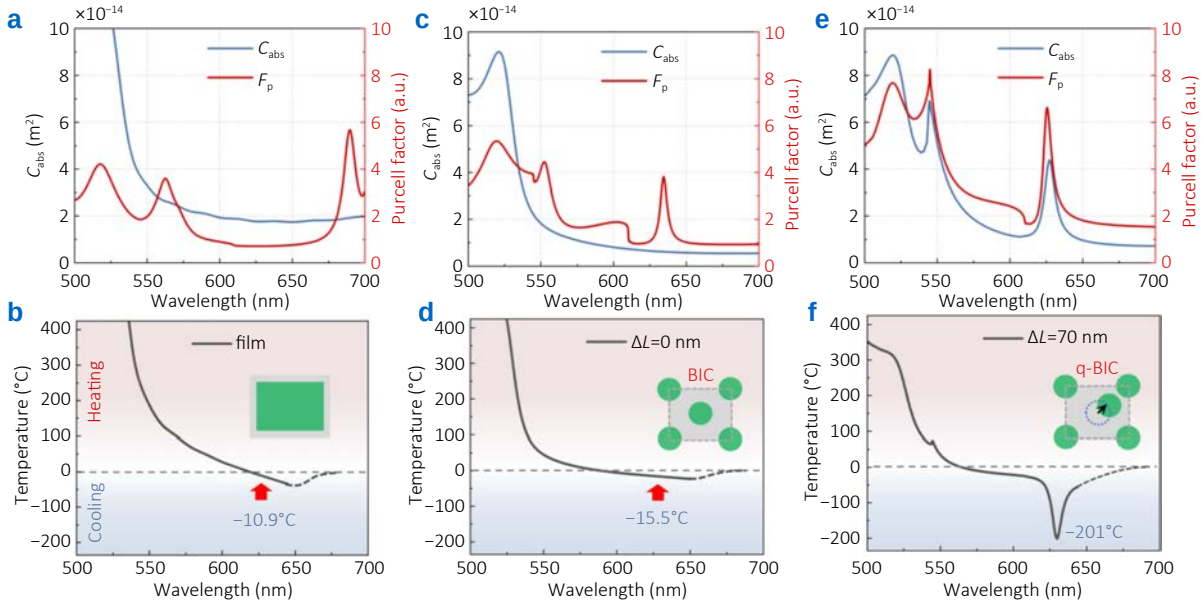

Fig. 4 | Comparison of optical response and refrigeration performance. (a, c, e) Absorption cross-section (C_{abs}, blue) and Purcell factor (F_P, red) spectra for (a) an unstructured perovskite film, (c) a BIC metasurface with ΔL = 0 nm, and (e) a dual q-BIC metasurface with ΔL = 70 nm. (b, d, f) Corresponding simulated temperature variation under 1.5×10⁵ W/cm² excitation, giving steady-state temperatures of −10.9 °C, −15.5 °C, and −201 °C for (a, c, e), respectively.

laser illumination (1.5×10⁵ W/cm²), it still shows a finite temperature reduction, reaching a steady-state temperature of −15.5 °C (Fig. 4(d)), which primarily originates from non-resonant background absorption associated with intrinsic material loss rather than quasi-BIC-enabled resonance enhancement. In contrast, the symmetry-broken dual-band q-BIC structure unlocks radiative channels and establishes spectrally matched excitation-emission resonances, leading to pronounced enhancement of both absorption cross-section and Purcell factor (Fig. 4(e)). This dual-band resonance synergy enables efficient photon recycling, which in simulations translates into cryogenic cooling to −201 °C (72 K, ΔT=226 °C from ambient environment), surpassing the liquid-nitrogen threshold of −196 °C. Compared to the unstructured film and the BIC metasurface, the optimized q-BIC design achieves more than an order-of-magnitude improvement in cooling performance. These results demonstrate that symmetry-engineered meta-atoms can reconfigure thermal radiation channels and modulate photonic density of states, thereby extending the design possibilities for optical refrigeration.

3 Conclusions

We have developed a dual q-BIC-engineered perovskite metasurface that unifies enhanced optical absorption and radiative cooling through high-Q resonance engineering. Full-wave electromagnetic simulations combined with thermodynamic modeling reveal a 2.4-fold increase in absorption cross-section (1.8 × 10⁻¹⁴ m² at 625 nm) compared to unpatterned perovskite films, together with a Purcell factor of 8.2 that supports efficient radiative cooling. Theoretical predictions indicate cryogenic temperature reduction to −201 °C (ΔT = 226 °C) under ambient conditions. By integrating resonant photonic design with thermal dynamics, this work establishes a framework for perovskite-based deep cryogenic cooling beyond the liquid nitrogen threshold. The proposed dual q-BIC mechanism establishes general design principles for extreme photothermal management in all-dielectric systems, offering a new paradigm in solid-state refrigeration for high-density photonic circuits and quantum photonic devices.

4 Methods

In the study of optical cooling enhanced by dual BIC resonance in nanoparticles, the methodology involves a comprehensive approach that integrates carrier dynamics, optical properties, and thermal analysis. Here is a detailed and logical summary of the methods used.

4.1 Carrier dynamics modeling

The process begins with modeling the carrier concentration within the material when subjected to laser irradiation. The total carrier concentrations for electrons (n) and holes (p) are calculated by summing the equilibrium concentrations (n_0 for electrons and p_0 for holes) and the photogenerated concentrations (Δn and Δp):

$$\begin{cases} n = n_0 + \Delta n \\ p = p_0 + \Delta p \end{cases}. \tag{1}$$

This provides a fundamental basis for evaluating the subsequent recombination and optical processes.

4.2 Recombination rates calculation

The radiative recombination rate ($R_{\rm rad}$) is proportional to the product of electron and hole densities. For lead halide perovskites, the photogenerated carrier concentration is larger than the equilibrium carrier concentration. Under the assumption $\Delta n \gg n_0, \Delta p \gg p_0$, the volumetric radiative recombination rate can be written as

$$R_{\rm rad} = B\Delta n\Delta p = BN^2 \,, \tag{2}$$

where $N = \Delta n = \Delta p$ is the laser-induced electron–hole carrier density, and B denotes the bimolecular recombination coefficient (unit: $\rm cm^3{\cdot}s^{-1}$). Non-radiative recombination ($R_{\rm nonrad}$) includes trap-assisted recombination and Auger processes, expressed as

$$R_{\rm nonrad} = AN + CN^3 \,, \tag{3}$$

with A and C the corresponding coefficients. For the present model, representative values are A=3×10^6 ($\rm cm^{-3}{\cdot}s^{-1}$), B=1×10^{-9} ($\rm cm^3{\cdot}s^{-1}$) and C=9×10^{-29} ($\rm cm^6{\cdot}s^{-1}$). These parameters should be adjusted according to experimental measurements or material-specific data[46].

Under continuous-wave (CW) steady-state excitation, the carrier density satisfies the rate equation:

$$\frac{{\rm d}N}{{\rm d}t} = 0 = G - AN - BN^2 - CN^3 \,, \tag{4}$$

where G is the photogeneration rate per unit volume. This generation term is set by the actual optical absorption of the nanostructure (see the absorption subsection below).

4.3 Optical absorption and photogeneration

The absorption properties of nanoparticles are characterized by the absorption cross-section $C_{\rm abs}$, defined as the ratio between absorbed power and incident intensity:

$$C_{\rm abs} = \frac{p_{\rm abs}}{I} \,. \tag{5}$$

The absorption cross-section $C_{\rm abs}$ depends on the structure's permittivity, geometry, excitation wavelength and collective scattering effects of the periodic arrangement. This quantity directly determines the carrier generation rate under laser pumping. The total photogeneration per unit volume is given by

$$G = \frac{IC_{\rm abs}}{\hbar w_{\rm i} V} \,, \tag{6}$$

where I is the incident intensity, $\hbar w_i$ is the pump photon energy, and V is the active volume of the nanoparticle. A larger $C_{\rm abs}$ at the pump wavelength therefore increases G, raises the steady-state carrier density N, and consequently modifies both radiative and non-radiative recombination rates.

4.4 Emission enhancement and Purcell factor

In a nanophotonic environment, the spontaneous emission rate can be enhanced by the Purcell factor $F_{\rm P}$, which effectively modifies the radiative term as

$$R_{\rm rad}^{\rm eff} = F_{\rm P}BN^2 \,. \tag{7}$$

Thus, the Purcell factor provides a direct link between optical mode confinement and the acceleration of spontaneous emission.

This enhancement improves the internal radiative efficiency:

$$\eta_{\rm rad} = EQE = \frac{R_{\rm rad}^{\rm eff}}{R_{\rm rad}^{\rm eff} + R_{\rm nonrad}} \,. \tag{8}$$

4.5 Cooling efficiency and temperature evolution

With the carrier dynamics and optical properties established, the optical cooling efficiency ($\eta_{\rm C}$) is calculated as the ratio of net cooling power to absorbed power:

$$\eta_{\rm C} = \frac{P_{\rm lum} - P_{\rm abs}}{P_{\rm abs}} = \eta_{\rm rad}\frac{\lambda_{\rm i}}{\lambda_{\rm PL}} - 1 \,. \tag{9}$$

Here, $P_{\rm lum}$ denotes the emitted power. The absorbed power is derived from $C_{\rm abs}$ and the incident light intensity. This framework can be further expressed in terms of the recombination rates and the photon energies of absorption and emission.

The steady-state temperature change ΔT is determined by balancing the net cooling power against heat conduction to the environment. For a spherical particle of radius R in a medium with thermal conductivity κ, the relation is

$$\Delta T = -\frac{\eta_{\rm C}C_{\rm abs}I}{4\pi\kappa R} \,, \tag{10}$$

where κ = 0.022 $\rm W{\cdot}m^{-1}{\cdot}K^{-1}$.

This methodology provides a thorough framework for understanding and optimizing the optical cooling process in nanoparticles. By considering the interplay between carrier generation, optical absorption and emission, and thermal transfer, it offers insights into enhancing cooling efficiency through the design and manipulation of nanophotonic structures.

4.6 Material parameters

In all electromagnetic simulations, the complex refractive index of $MAPbBr_3$, $n(\lambda)$ + i$k(\lambda)$, as shown in Fig. 5, was adopted from the experimental optical constants reported previously[47].

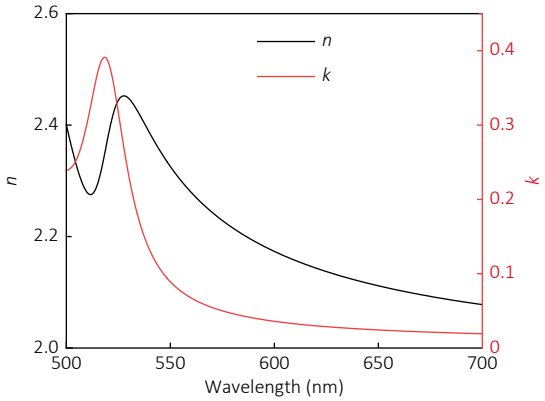

Fig. 5 | Optical constants of $MAPbBr_3$ used in the simulations. Wavelength-dependent refractive index $n(\lambda)$ (gray curve, left axis) and extinction coefficient $k(\lambda)$ (red curve, right axis) over the spectral range relevant to this work.

References

1. Sheik-Bahae M, Epstein RI. Laser cooling of solids. *Laser Photon Rev* **3**, 67–84 (2009).
2. Hehlen MP, Sheik-Bahae M, Epstein RI. Solid-state optical refrigeration. *Handbook Phys Chem Rare Earths* **45**, 179–260 (2014).
3. Seletskiy DV, Epstein R, Sheik-Bahae M. Laser cooling in solids: advances and prospects. *Rep Prog Phys* **79**, 096401 (2016).
4. Sheik-Bahae M, Epstein RI. Optical refrigeration. *Nat Photon* **1**, 693–699 (2007).
5. Pringsheim P. Zwei bemerkungen über den unterschied von lumineszenz- und temperaturstrahlung. *Z Physik* **57**, 739–746 (1929).
6. Epstein RI, Buchwald MI, Edwards BC et al. Observation of laser-induced fluorescent cooling of a solid. *Nature* **377**, 500–503 (1995).
7. Mungan CE, Buchwald MI, Edwards BC et al. Laser cooling of a solid by 16 K starting from room temperature. *Phys Rev Lett* **78**, 1030–1033 (1997).
8. Hoyt CW, Sheik-Bahae M, Epstein RI et al. Observation of anti-Stokes fluorescence cooling in thulium-doped glass. *Phys Rev Lett* **85**, 3600–3603 (2000).
9. Hoyt CW, Hasselbeck MP, Sheik-Bahae M et al. Advances in laser cooling of thulium-doped glass. *J Opt Soc Am B* **20**, 1066–1074 (2003).
10. Fernández J, Mendioroz A, García AJ et al. On the origin of anti-Stokes laser-induced cooling of Yb^{3+}-doped glass. *Opt Mater* **16**, 173–179 (2001).
11. Peysokhan M, Rostami S, Mobini E et al. Implementation of laser-induced anti-Stokes fluorescence power cooling of ytterbium-doped silica glass. *ACS Omega* **6**, 8376–8381 (2021).
12. Melgaard SD, Albrecht AR, Hehlen MP et al. Solid-state optical refrigeration to sub-100 Kelvin regime. *Sci Rep* **6**, 20380 (2016).
13. Melgaard S. Cryogenic optical refrigeration: laser cooling of solids below 123 K (The University of New Mexico, Albuquerque, 2013).
14. Zhang J, Li DH, Chen RJ et al. Laser cooling of a semiconductor by 40 kelvin. *Nature* **493**, 504–508 (2013).
15. Dabbousi BO, Rodriguez-Viejo J, Mikulec FV et al. (CdSe)ZnS core-shell quantum dots: synthesis and characterization of a size series of highly luminescent nanocrystallites. *J Phys Chem B* **101**, 9463–9475 (1997).
16. Jung D, Park JW, Min S et al. Strain-graded quantum dots with spectrally pure, stable and polarized emission. *Nat Commun* **15**, 5561 (2024).
17. Yamada Y, Oki T, Morita T et al. Optical cooling of dot-in-crystal halide perovskites: challenges of nonlinear exciton recombination. *Nano Lett* **24**, 11255–11261 (2024).
18. Pokryshkin NS, Mantsevich VN, Timoshenko VY. Anti-Stokes photoluminescence in halide perovskite nanocrystals: from understanding the mechanism towards application in fully solid-state optical cooling. *Nanomaterials* **13**, 1833 (2023).
19. Ha ST, Shen C, Zhang J et al. Laser cooling of organic-inorganic lead halide perovskites. *Nature Photon* **10**, 115–121 (2016).
20. As'ham K, Al-Ani I, Lei W et al. Mie exciton-polariton in a perovskite metasurface. *Phys Rev Appl* **18**, 014079 (2022).
21. Baryshnikova K, Gets D, Liashenko T et al. Broadband antireflection with halide perovskite metasurfaces. *Laser Photon Rev* **14**, 2000338 (2020).
22. Fan YB, Wang YH, Zhang N et al. Resonance-enhanced three-photon luminesce via lead halide perovskite metasurfaces for optical encoding. *Nat Commun* **10**, 2085 (2019).
23. Gan ZX, Cheng YC, Chen WJ et al. Photophysics of 2D organic-inorganic hybrid lead halide perovskites: progress, debates, and challenges. *Adv Sci* **8**, 2001843 (2021).
24. Cheng YH, Du J, Wang W. Enhancement of strong intrinsic light-matter interaction in a perovskite metasurface embedded in an optical cavity. *Phys Rev B* **112**, 085424 (2025).
25. Protesescu L, Yakunin S, Bodnarchuk MI et al. Nanocrystals of cesium lead halide perovskites ($CsPbX_3$, X=Cl, Br, and I): novel optoelectronic materials showing bright emission with wide color gamut. *Nano Lett* **15**, 3692–3696 (2015).
26. Wang HL, Haroldson R, Balachandran B et al. Nanoimprinted perovskite nanograting photodetector with improved efficiency. *ACS Nano* **10**, 10921–10928 (2016).
27. Schmager R, Gomard G, Richards BS et al. Nanophotonic perovskite layers for enhanced current generation and mitigation of lead in perovskite solar cells. *Sol Energy Mater Sol Cells* **192**, 65–71 (2019).
28. Cheng PF, An YD, Jen AKY et al. New nanophotonics approaches for enhancing the efficiency and stability of perovskite solar cells. *Adv Mater* **36**, 2309459 (2024).
29. Tiguntseva E, Koshelev K, Furasova A et al. Room-temperature lasing from Mie-resonant nonplasmonic nanoparticles. *ACS Nano* **14**, 8149–8156 (2020).
30. Liu CC, Hsiao HH, Chang YC. Nonlinear two-photon pumped vortex lasing based on quasi-bound states in the continuum from perovskite metasurface. *Sci Adv* **9**, eadf6649 (2023).
31. Wang RZ, Su Y, Fan HJ et al. Tunable vertical cavity microlasers based on $MAPbI_3$ phase change perovskite. *Opto-Electron Adv* **8**, 240220 (2025).
32. Kodigala A. Lepetit T, Gu Q et al. Lasing action from photonic bound states in continuum. *Nature* **541**, 196–199 (2017).
33. Koshelev K, Lepeshov S, Liu MK et al. Asymmetric metasurfaces with high-Q resonances governed by bound states in the continuum. *Phys Rev Lett* **121**, 193903 (2018).
34. Hsu CW, Zhen B, Stone AD et al. Bound states in the continuum.

Nat Rev Mater **1**, 16048 (2016).
35. Fan KB, Shadrivov IV, Padilla WJ. Dynamic bound states in the continuum. *Optica* **6**, 169–173 (2019).
36. Doeleman HM, Monticone F, den Hollander W et al. Experimental observation of a polarization vortex at an optical bound state in the continuum. *Nat Photon* **12**, 397–401 (2018).
37. Li ZC, Liu WW, Zhang YB et al. Optical polarization manipulations with anisotropic nanostructures. *PhotoniX* **5**, 30 (2024).
38. Moretti GQ, Weber T, Possmayer T et al. Si metasurface supporting multiple quasi-BICs for degenerate four-wave mixing. *Nanophotonics* **13**, 3421–3428 (2024).
39. Wang ZH, Zheng YB, Ouyang M et al. High-*Q* quasi-bound states in the continuum in C_2-symmetric metasurface with enhanced second harmonic generation in two-dimensional materials. *Opt Laser Technol* **176**, 110868 (2024).
40. Zheng YH, Tang X, Xu MF et al. High-order rotational symmetry induced high-*Q* generalized geometric phases in nonlocal metasurfaces. *Laser Photon Rev*, e02322 (2025).
41. Jia TX, Jeon Y, Feng L et al. Superchirality induced ultrasensitive chiral detection in high-*Q* optical cavities. *Opto-Electron Adv* **8**, 250079 (2025).
42. He HY, Lai FX, Zhang Y et al. Spectro-polarimetric detection enabled by multidimensional metasurface with quasi-bound states in the continuum. *Opto-Electron Adv* **8**, 250015 (2025).
43. Tonkaev P, Zograf G, Makarov S. Optical cooling of lead halide perovskite nanoparticles enhanced by Mie resonances. *Nanoscale* **11**, 17800–17806 (2019).
44. Nemova G, Kashyap R. Laser cooling of solids. *Rep Prog Phys* **73**, 086501 (2010).
45. Chuang SL, Peyghambarian N, Koch S. Physics of optoelectronic devices. *Phys Today* **49**, 62 (1996).
46. Johnston MB, Herz LM. Hybrid perovskites for photovoltaics: charge-carrier recombination, diffusion, and radiative efficiencies. *Acc Chem Res* **49**, 146–154 (2016).
47. Brittman S, Garnett EC. Measuring *n* and *k* at the microscale in single crystals of $CH_3NH_3PbBr_3$ perovskite. *J Phys Chem C* **120**, 616–620 (2016).

Acknowledgements

This work was supported by the National Key R&D Program of China (2024YFA1209301, 2022YFB3607300), the National Natural Science Foundation of China (NSFC) (62075084, 62325503, 62005104, 12404432，62575032, 62475102), the Guangdong Province Basic and Applied Basic Research Foundation (2025A1515012110), the Fund of State Key Laboratory of Information Photonics and Optical Communications (BUPT) (2024ZT03), P. R. China, and the China Postdoctoral Science Foundation (2025M770804).

Competing interests

The authors declare no competing financial interests.